The Meteoritical Society

Meteoritics & Planetary Science 51, Nr 2, 372–389 (2016)
doi: 10.1111/maps.12596

First finding of impact melt in the IIE Netschaëvo meteorite

N. VAN ROOSBROEK[1,2*], L. PITTARELLO[2], A. GRESHAKE[3], V. DEBAILLE[1], and P. CLAEYS[2]

[1]Laboratoire G-Time, Université Libre de Bruxelles, CP 160/02, 50 Avenue F. D. Roosevelt, B-1050 Brussels, Belgium
[2]Analytical, Environmental, and Geo-Chemistry (AMGC), Vrije Universiteit Brussel, Pleinlaan 2, B-1050 Brussels, Belgium
[3]Museum für Naturkunde, Leibniz-Institut für Evolutions- und Biodiversitätsforschung, Invalidenstraße 43, 10115 Berlin, Germany
[*]Corresponding author. E-mail: nadia.van.roosbroek@ulb.ac.be

(Received 18 May 2015; revision accepted 10 November 2015)

Abstract–About half of the IIE nonmagmatic iron meteorites contain silicate inclusions with a primitive to differentiated nature. The presence of preserved chondrules has been reported for two IIE meteorites so far, Netschaëvo and Mont Dieu, which represent the most primitive silicate material within this group. In this study, silicate inclusions from two samples of Netschaëvo were examined. Both silicate inclusions are characterized by a porphyritic texture dominated by clusters of coarse-grained olivine and pyroxene, set in a fine-grained groundmass that consists of new crystals of olivine and a glassy appearing matrix. This texture does not correspond to the description of the previously examined pieces of Netschaëvo, which consist of primitive chondrule-bearing angular clasts. Detailed petrographic observations and geochemical analyses suggest that the investigated samples of Netschaëvo consist of quenched impact melt. This implies that Netschaëvo is a breccia containing metamorphosed and impact-melt rock (IMR) clasts and that collisions played a major role in the formation of the IIE group.

INTRODUCTION

The formation of the majority of iron meteorites can be explained by fractional crystallization of slowly cooling metallic liquids (Scott 1972; Choi et al. 1995), indicating that they originated from the core of differentiated bodies. These meteorites belong to the magmatic or fractionally crystallized groups (IC, IIAB, IIC, IID, IIIAB, IIIE, IIIF, IVA, and IVB). However, the formation of several other iron meteorites, frequently containing silicate inclusions, cannot be explained by fractional crystallization alone (Goldstein et al. 2009). These nonmagmatic or silicate-bearing iron meteorites consist of the IAB complex and IIE.

Among the nonmagmatic iron meteorites, the metal phase of the IIE iron meteorites shows characteristics that distinguish them from the other silicate-bearing groups: (1) a much smaller Ni range (7.2–9.5 wt% for IIE versus 6–60 wt% for the IAB complex), (2) higher As/Ni and Au/Ni ratios, (3) the absence of carbon, and (4) minor amounts of FeS (Wasson and Wang 1986; Choi et al. 1995). About half of the IIE irons contain silicate inclusions that present a wide variety of characteristics, ranging from large chondritic clasts to smaller molten feldspar-rich globules (Ruzicka 2014). Mittlefehldt et al. (1998) classified silicate-bearing IIE on the basis of the features in the inclusions, from the most primitive (1) to the most differentiated material (5). The first subgroup contains silicate inclusions with preserved chondritic texture and mineralogy. Such angular chondritic clasts that contain preserved chondrules were first found in the IIE iron meteorite Netschaëvo and the meteorite was, thus, chosen to represent subgroup (1) (Olsen and Jarosewich 1971). Until recently this meteorite was also the only member of subgroup (1). Van Roosbroek et al. (2015) proposed that Mont Dieu, a IIE iron containing primitive chondrule-bearing cm-sized silicate inclusions, might also be a member of subgroup (1). The other silicate-bearing IIE meteorites are classified in: subgroup (2), e.g., Techado, with silicate inclusions with chondritic bulk composition but without chondritic textures (Casanova et al. 1995); subgroup (3), e.g., Watson, with a chondritic inclusion that has lost its metal and sulfide

© The Meteoritical Society, 2016.

(Olsen et al. 1994); subgroup (4), e.g., Miles and Weekeroo Station, with globular silicate inclusions containing orthopyroxene, clinopyroxene and plagioclase (Bunch and Olsen 1968; McCoy 1995); and subgroup (5), e.g., Colomera, Kodaikanal, and Elga, with globular inclusions dominated by clinopyroxene and glass (Prinz et al. 1980).

Several lines of evidence suggest that IIE irons are genetically related to H chondrites. The most important arguments are the overlap between the oxygen isotope compositions of IIE silicates and H chondrites (Clayton and Mayeda 1996); the chondritic textures and mineralogy present in the unfractionated IIE, such as Mont Dieu, Netschaëvo, and Techado (Olsen and Jarosewich 1971; Casanova et al. 1995; Van Roosbroek et al. 2015); and the metal phase of IIE that has a similar composition as the metal found in H chondrites (Wasson and Wang 1986). Although several characteristics of IIE silicates and H chondrites overlap, others do not exactly match, leading several authors to suggest that they did not originate on the main H chondrite asteroid, but on a related, H-chondrite-like parent body (Bogard et al. 2000). Bild and Wasson (1977) and Rubin (1990) supported this idea, based on their studies of Netschaëvo. According to these authors, several characteristics such as the Fa content in olivine, Co concentration in kamacite, and oxygen isotopic composition, indicate that Netschaëvo is derived from a more iron-rich parent body than the H chondrites, that they call the HH parent body (Bild and Wasson 1977; Rubin 1990).

Radiometric ages divide the silicate-bearing IIE iron meteorites into two groups that do not correspond to the above-mentioned mineralogical subdivision. An "old" IIE group, with IIE having a formation age of ~4.5 Ga, consists of 6 meteorites: Weekeroo Station, Colomera, Miles, Techado (Bogard et al. 2000), Taramuhara (Takeda et al. 2003b), and the recently described Mont Dieu (Van Roosbroek et al. 2015) and a "young" group consisting of Netschaëvo, Kodaikanal, and Watson sharing ages of around 3.6 Ga (Bogard et al. 2000).

Over the past decades, several formation scenarios have been proposed for the IIE iron meteorites, to account for all their different features. These scenarios can be subdivided into exogenic, endogenic, and hybrid models. In exogenic models, IIE are formed by impact mixing and partial to complete impact melting (Burnett and Wasserburg 1967; Bence and Burnett 1969; Scott and Wasson 1976; Osadchii et al. 1981; Rubin et al. 1986; Wasson and Wang 1986; Olsen et al. 1994; Ikeda and Prinz 1996; Ikeda et al. 1997; Van Roosbroek et al. 2015). In endogenic models IIE formed by incomplete separation of metal and troilite from silicate during internal heating on their parent asteroid (Wasserburg et al. 1968; Prinz et al. 1982; McCoy 1995). Hybrid models consist of a combination of both extremes (Bunch et al. 1970; Armstrong et al. 1990; Casanova et al. 1995; Ruzicka et al. 1999; Bogard et al. 2000; Hsu 2003; Takeda et al. 2003a, 2003b; Ruzicka and Hutson 2010). Ruzicka (2014) subdivided them in three groups (1) "cold crust models" where metallic melt is mixed with cold silicate fragments at the surface of an asteroid as a consequence of an impact event; (2) "hot mixing models" where metallic melt is injected, as a consequence of an impact event, in a chondritic body that was internally heated; and (3) "collisional disruption and reaccretion" models where the internally heated parent body broke up and reaccreted afterward. All these formation models involve a chondritic parent body that is either identical or related to the H chondrite parent body.

In this study, we present a detailed petrographic and geochemical investigation of two samples of Netschaëvo, with the main focus on the silicate inclusions showing textures that do not correspond to the previously described silicate inclusions found in Netschaëvo. Its formation process and the history of its parent body are discussed.

SAMPLES DESCRIPTION AND ANALYTICAL TECHNIQUES

We examined two samples of Netschaëvo IIE, one from the Natural History Museum in London (Fig. 1a), United Kingdom (registration number: BM. 33953), and one from the Museum für Naturkunde in Berlin, Germany (registration number: Meteorite collection Inv-Nr. 1907). Both samples contain a cm-sized silicate inclusion embedded in a metal mass. The sample from Berlin is a metallic block of about 6 × 4 cm and 1 cm thick. It contains an elongated silicate inclusion of about 5.5 cm long and 1.5 cm thick. The sample from London is about 13 × 12 mm and consists of a silicate inclusion of about 10 × 8 mm surrounded by metal. The two silicate inclusions show the same textures and are not similar to the chondrule-bearing clasts previously reported in Netschaëvo (Olsen and Jarosewich 1971). Polished sections have been prepared from each of these samples: in one case only from the silicate inclusion, in the other case from the silicate inclusion as well as from the surrounding metal host. Both samples were examined with scanning electron microscopy (SEM), electron microprobe, and Raman spectroscopy.

Backscattered electron imaging was performed at the Vrije Universiteit Brussel (VUB) using a JEOL-JSM7000F Field Emission SEM with Schottky type

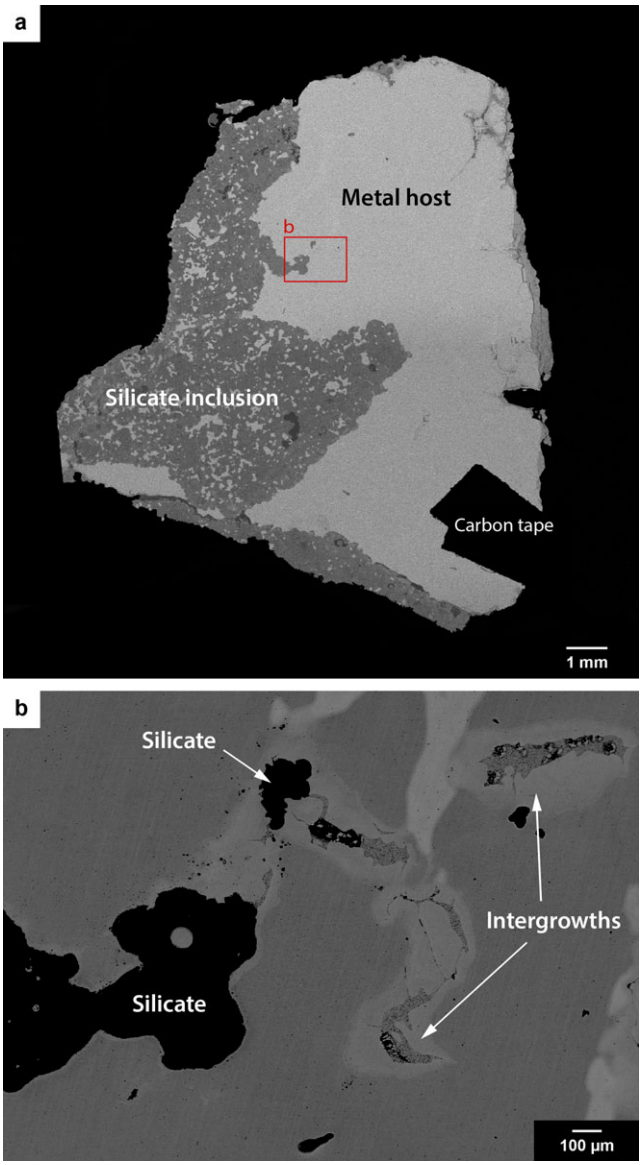

Fig. 1. a) Backscattered electron image showing one (from the Natural History Museum in London) of the investigated samples of Netschaëvo. b) Metal host showing the metal–phosphorus–sulfur intergrowths connected to the silicate inclusion.

tungsten emitter and a theoretical lateral resolution of 1.2 nm. Modal abundances were defined using ImageJ free software on four backscattered SEM (BSE-SEM) images, collected at different magnification, covering areas corresponding to ~0.5 mm^2, 2 mm^2, and 2 times 4 mm^2. The volume content of selected minerals was estimated from the area percentage in the analyzed images, following a revised version of the technique described by Heilbronner (2000). The modes obtained can be considered as representative of the real volume distribution by stereological assumptions (Underwood 1970). The term "opaque phases" is used to refer to those minerals that appear opaque in transmitted light using optical microscopy, although they are investigated by electron microscopy in this study.

Backscattered electron images, quantitative mineral analyses, mineral traverses, and X-ray elemental maps were obtained with a JEOL JXA 8500F field emission cathode electron microprobe (Museum für Naturkunde, Berlin) equipped with five wavelength-dispersive spectrometers (WDS) and one energy-dispersive spectrometer (EDS) using 10–15 kV accelerating voltage, 15 nA beam current, and 1–5 µm beam sizes. For the electron microprobe traverses (step size = 1 µm), only measurements fitting the mineral formula were taken into account to avoid contamination from the matrix material. Suitable mineral standards including anorthoclase; basaltic glass; chromite; chromium augite; diopside; ilmenite; microcline; plagioclase; pentlandite; and metal standards of Co, Fe, and Ni, all certified by the National Museum of Natural History (United States) as reference samples for electron microprobe analysis (Jarosewich et al. 1980), were applied to calculate mineral compositions.

Raman spectroscopy was carried out at the VUB using a LabRAM HR Evolution (HORIBA Scientific) confocal Raman spectrometer and the LabSpec software. This instrument is equipped with a high-stability confocal microscope with XYZ motorized stage, a number of different objectives (WD = 10.6 mm), and a multichannel air-cooled CCD detector (spectral resolution <1 cm^{-1}, lateral resolution 0.5 µm, axial resolution 2 µm). Raman spectra were excited with solid-state green laser (532 nm wavelength; ~6.25 mW power).

RESULTS

Metal Host

The metal surrounding the silicate inclusion in one of the investigated samples of Netschaëvo is mainly composed of kamacite and shows no Widmanstätten pattern. Irregularly shaped and elongated inclusions of taenite (up to 1 mm long and 500 µm wide) occur randomly spread in the kamacite groundmass. Within these taenite areas, elongated intergrowths with a diameter of a few hundred µm were found consisting of (sub)rounded Fe-Ni blebs of 10–50 µm surrounded by a dense interstitial dendritic network (Fig. 2a). This network is a mixture of Fe-Ni metal blebs or dendrites (1–5 µm), set in a groundmass of a P-rich and a S-rich phase. Some of these intergrowths are associated with troilite that contains abundant round blebs of Fe-Ni metal (Fig. 2a). The taenite-rich areas, containing the

described intergrowths, are connected to each other, forming a network within the kamacite host and, are locally also connected to the silicate inclusion (Fig. 1b). The contact between the metal host and the silicate inclusion is smooth and rounded, and the border of the silicate is locally rimmed by troilite.

Silicate Inclusions

The silicate inclusions are characterized by a porphyritic texture dominated by coarse-grained olivine, and to a lesser extent, pyroxene crystals. They are embedded in a groundmass of fine-grained euhedral olivine crystals set in a matrix, which is partially crystallized showing microlitic domains consisting of olivine (Figs. 2b and 3). Image analysis reveals that the inclusions consist of about 28 vol% coarse-grained olivines, 16 vol% coarse-grained pyroxenes, 39 vol% fine-grained material (matrix and fine-grained olivines), and 18 vol% opaque phases. One possible relict chondrule was observed in one of the sections (Fig. 2c).

Coarse-Grained Olivine and Pyroxene Grains

Coarse-grained olivine and pyroxene crystals occur as clusters of about 400–500 μm and consist of individual crystals ranging from 20 to 200 μm, which commonly exhibit a compositionally homogeneous core and zoned rim. The boundary between core and rim is sharp and is easily identified in BSE images by the different gray shades. The core generally has a subrounded to amoeboid shape and the 1–15 μm thick rim either roughly mimics the shape of the core or exhibits a hypidiomorphic shape (Figs. 3b and 3c). The cores of the coarse-grained olivine and pyroxene grains are locally fractured (Figs. 3b and 3c). Compositionally, the cores of the coarse-grained olivine grains appear to be homogeneous in composition, corresponding to $Fa_{14.3 \pm 0.3}$, whereas the rim is Fe-rich ($Fa_{29.3 \pm 4.0}$, Table 1; Fig. 4). The cores of the coarse-grained low-Ca pyroxene crystals have a homogeneous composition of $En_{84.0 \pm 0.4}$ $Fs_{14.8 \pm 0.3}$ $Wo_{1.2 \pm 0.3}$. The rims of these grains have an average composition of $En_{72.0 \pm 2.8}$ $Fs_{25.9 \pm 2.3}$ $Wo_{2.1 \pm 0.6}$. The rims appear progressively enriched in Ca and Fe toward the edge (Table 1; Fig. 4). Locally, where the pyroxene rims are thicker, the composition of the outer part of the rim falls in the field of pigeonite ($En_{59.7 \pm 3.6}$ $Fs_{32.7 \pm 1.0}$ $Wo_{7.6 \pm 2.7}$) (Table 1; Fig. 4).

Clusters of Fine-Grained Olivine and Pyroxene

Clusters of fine-grained olivine or pyroxene crystals are found heterogeneously distributed within the silicate inclusion. Pyroxene clusters are ~30–60 μm in diameter and consist of few locally aligned crystals up to 4 μm in

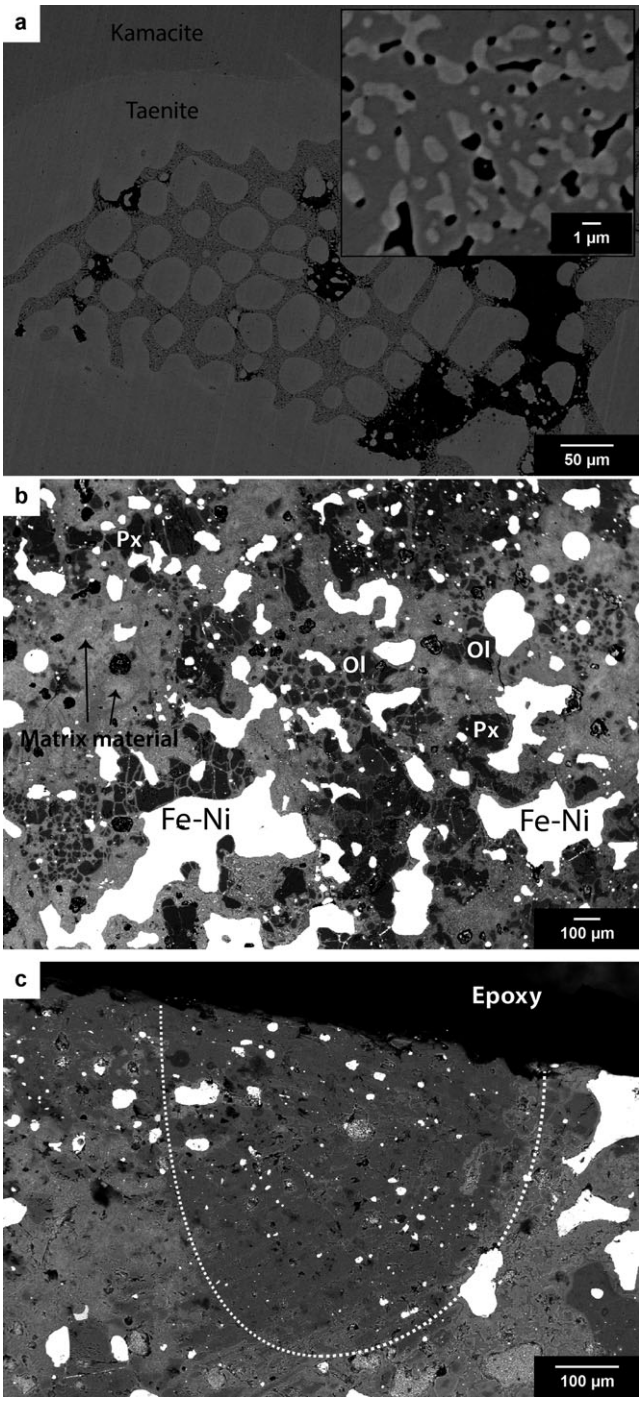

Fig. 2. Backscattered electron images showing the overall petrographic features of Netschaëvo. a) Metal host showing the kamacite groundmass with metal–phosphorus–sulfur intergrowths surrounded by taenite. The inset shows the intergrowth texture of a S-rich phase (black), a P-rich phase (gray), and Fe-Ni dendrites (white). b) Silicate inclusion showing the clusters of olivine (Ol) and pyroxene (Px) set in a fine-grained matrix consisting of smaller secondary olivine crystals and glassy-like material. c) The outline of the possible chondrule is marked with a dotted line.

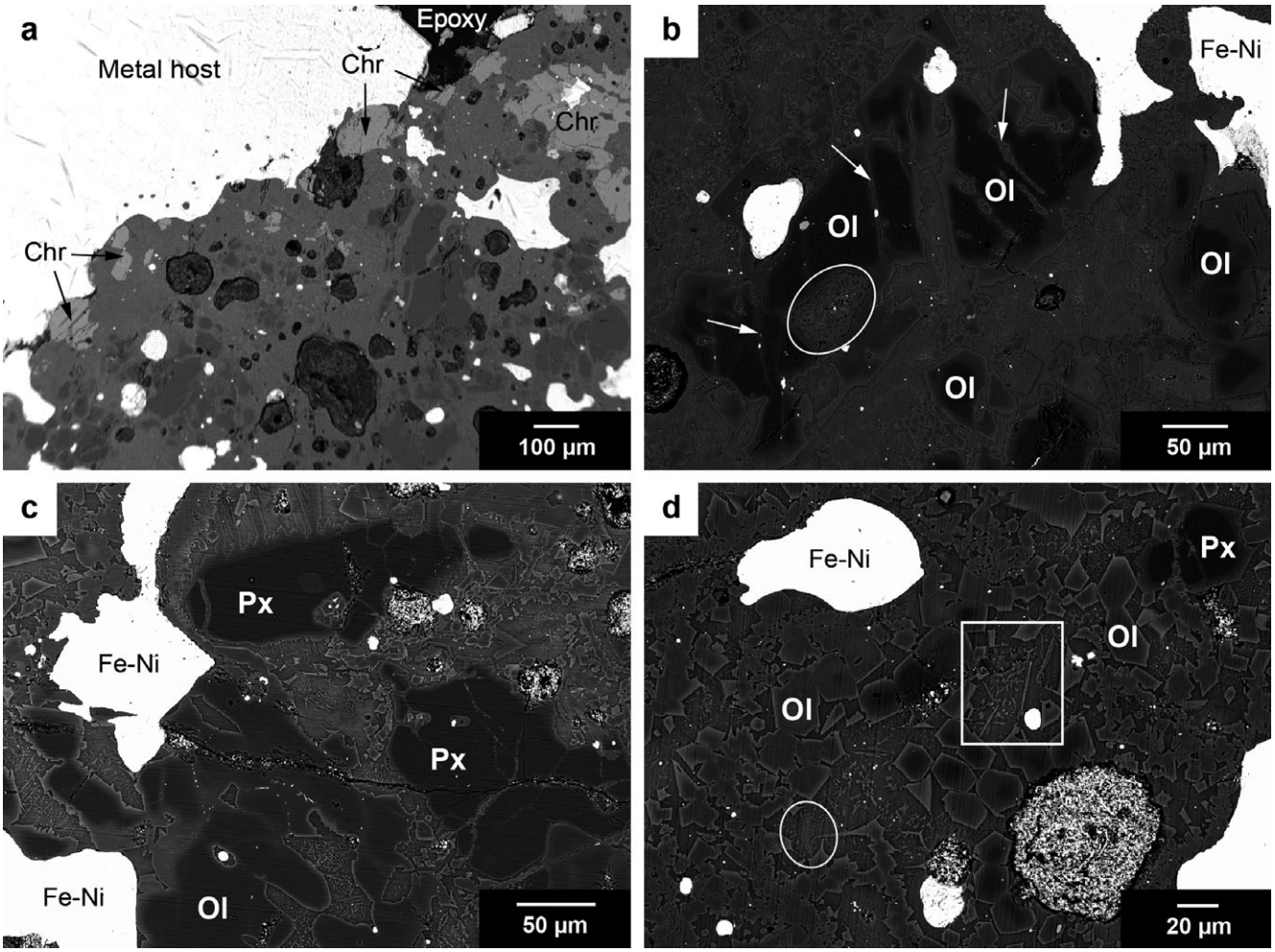

Fig. 3. Backscattered electron images showing the overall petrographic features of the silicate inclusions in Netschaëvo. a) Boundary between metal and silicate inclusion showing abundant chromite crystals (Chr) close to the metal-silicate contact. b) Large fractured (arrows) relict olivine grains (Ol) displaying irregular ferroan rims and partly engulfing matrix material (circle). c) Relict olivine (Ol) and pyroxene (Px) grains with irregular rim. Large irregular metal grains (Fe-Ni) and small metal blebs are spread in the matrix. d) Enlarged view of the glassy-like matrix material with hopper olivines, feathery olivines (circle), pockets of matrix material with rod olivine morphologies (square), and a small cluster of pyroxene grains (Px) with irregularly shaped rims.

size (Fig. 3d). The core of the small crystals is generally (sub)rounded while the rim of ~ 5–10 µm is euhedral. Locally the rim can be as thick or even thicker than the core, but this might be a 3-D effect of sectioning. These small pyroxene crystals show a compositionally homogeneous core and a compositionally zoned rim that can be clearly distinguished, corresponding to the core/rim compositions of the large pyroxene crystals described above.

An electron microprobe traverse across a pyroxene grain from core to rim shows that FeO and MgO display an anticorrelated trend, i.e., FeO increases toward the rim while MgO decreases (Fig. 5). CaO and Cr_2O_3 are zoned in the rim (Fig. 5) and show the same behavior as FeO, with their concentration increasing toward the edge of the crystal. A decrease in concentration is observed for MnO and TiO_2, following the trend observed for MgO (Fig. 5). These trends are also present in the rim of the coarse-grained pyroxenes.

Olivine clusters consist of 20–40 µm sized hypidiomorphic crystals (Fig. 3d) with a subhedral to euhedral shaped rim about 1–2 µm in thickness. Locally the rim is as thick as 5–10 µm, possibly due to the 3-D effect of sectioning. The grains are compositionally zoned showing a forsteritic core and a fayalitic rim corresponding to the same composition of the cores and rims of the coarse-grained olivines. Although the compositions match, the core-rim structure is less clear and the chemical transition is more gradual for the fine-grained olivines compared to the coarse-grained olivines. Smaller olivine crystals (<20 µm) with a hypidiomorphic shape exhibit no clear distinction

Table 1. Average composition and standard deviation (2σ) of the silicates and chromite in Netschaëvo (wt%) measured by electron microprobe.

	Olivine core	Olivine rim	Fine-grained olivine	Low-Ca pyroxene core	Low-Ca pyroxene rim	Pigeonite	Chromite
SiO_2	40.6 ± 0.3	37.9 ± 1.0	38.9 ± 1.1	56.4 ± 1.8	54.6 ± 0.9	52.3 ± 1.4	–
TiO_2	<0.02	<0.03	<0.02	0.2 ± 0.03	<0.05	0.1 ± 0.1	2.1 ± 0.3
Al_2O_3	<0.04	0.1 ± 0.02	0.2 ± 0.05	0.3 ± 0.05	0.6 ± 0.2	1.7 ± 0.8	7.9 ± 0.2
Cr_2O_3	<0.04	0.6 ± 0.2	0.3 ± 0.2	0.2 ± 0.03	0.4 ± 0.2	1.1 ± 0.4	55.6 ± 1.1
FeO	13.6 ± 0.3	25.9 ± 2.7	21.9 ± 2.9	9.5 ± 0.2	16.5 ± 1.5	19.6 ± 2.0	26.8 ± 1.0
MnO	0.3 ± 0.07	0.2 ± 0.03	0.2 ± 0.1	0.4 ± 0.03	0.3 ± 0.04	0.3 ± 0.02	0.4 ± 0.05
MgO	45.5 ± 0.4	35.0 ± 2.4	37.9 ± 3.1	31.7 ± 1.1	26.2 ± 1.5	20.4 ± 3.8	5.04 ± 0.2
CaO	<0.05	0.3 ± 0.09	0.3 ± 0.2	0.6 ± 0.2	1.1 ± 0.4	3.6 ± 2.1	–
Na_2O	<0.01	<0.04	<0.06	<0.04	<0.05	0.1 ± 0.1	–
K_2O	<0.01	< 0.01	<0.01	<0.01	<0.02	<0.03	–
ZnO	–	–	–	–	–	–	0.2 ± 0.06
V_2O_3	–	–	–	–	–	–	0.8 ± 0.04
Total	100.2	100.1	99.9	99.4	99.8	99.3	99.8
Endmember	$Fa_{14.3 \pm 0.3}$	$Fa_{29.3 \pm 4.0}$	$Fa_{24.5 \pm 3.8}$	$Fs_{14.8 \pm 0.5}$ $Wo_{1.2 \pm 0.4}$	$Fs_{25.9 \pm 2.7}$ $Wo_{2.1 \pm 0.8}$	$Fs_{32.7 \pm 1.5}$ $Wo_{7.6 \pm 3.8}$	
No. of analyses	9	6	17	31	30	5	37

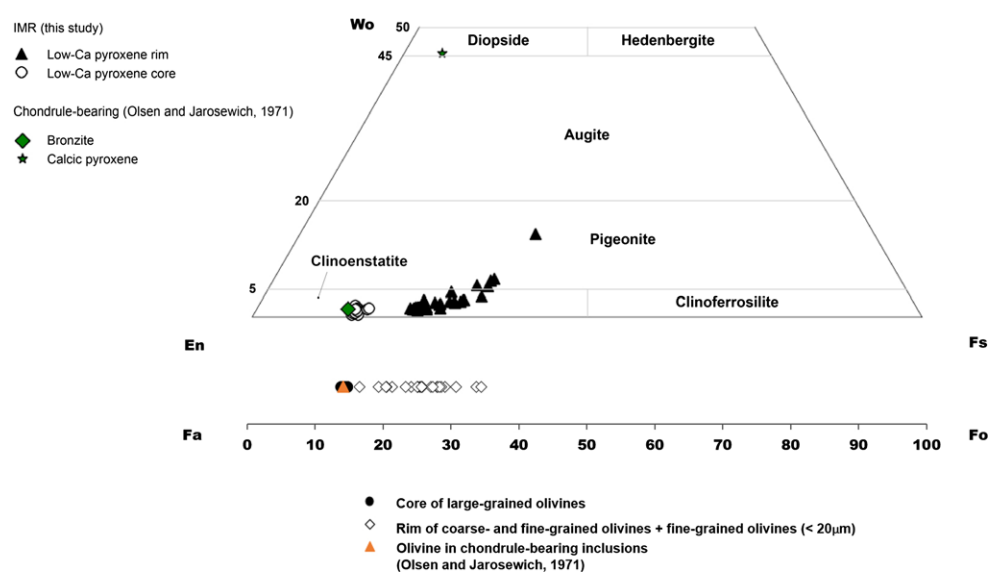

Fig 4. Composition of pyroxene (coarse- and fine-grained pyroxenes show the same trend in composition between the core and the rim) and olivine (the cores of the large-grained olivine plot in a narrow field while the composition of the rims of coarse- and fine-grained olivine plus the fine-grained olivines (<20 μm) without clear distinction between core and rim display a large range) in the investigated silicate inclusions and in the chondrule-bearing silicate clasts of Netschaëvo. All data in mole%. Limits of mineral fields from Deer et al. (1992).

between a core and a rim, but display a gradually lower Mg/Fe ratio toward the margin of the crystals, with a composition ranging from $Fa_{20.4}$ to $Fa_{30.7}$.

An electron microprobe traverse across a fine-grained olivine grain from rim to rim shows that FeO and MgO display an opposite trend: FeO is enriched in the rim while MgO is enriched in the core (Fig. 6). The change in Fe/Mg ratio can be evaluated qualitatively in BSE-SEM images, as the rim appears progressively brighter than the core. The rims of fine- and coarse-grained olivines have a higher amount of Cr_2O_3 and CaO (0.3 ± 0.2 wt% and 0.6 ± 0.2 wt%, respectively for Cr_2O_3; 0.3 ± 0.2 wt% and 0.3 ± 0.09 wt%, respectively for CaO) compared to the cores of those olivines (<0.04 for Cr_2O_3 and <0.05 for CaO) (Table 1). Minor elements such as Cr_2O_3 and CaO display the

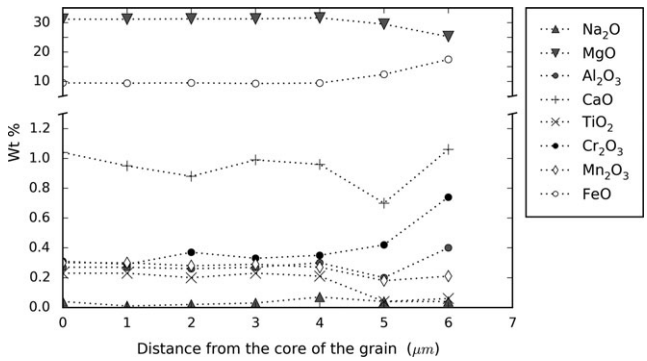

Fig. 5. Electron microprobe traverse from core to rim of a pyroxene grain. The rim is enriched in Fe, Ca, Cr, and depleted in Mg and Mn relative to the core.

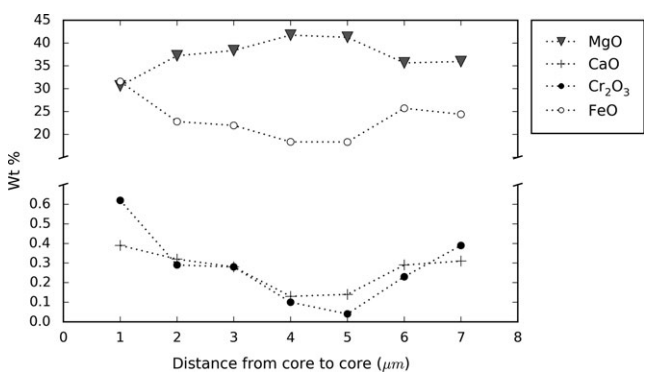

Fig. 6. Electron microprobe traverse across a secondary olivine grain. The rim of the newly crystallized olivine is enriched in Fe, Ca, and Cr and depleted in Mg relative to the core.

same trend as FeO in these grains, with a higher concentration in the rim and the lowest concentration in the core (Fig. 6).

The Matrix

The groundmass mostly appears glassy but locally displays different mineralogy and textures (Fig. 7) (1) matrix without dendrites; (2) with dendritic olivine (Fig. 3d); (3) with closely packed olivine dendrites, apparently without glassy material (Fig. 7a); and (4) matrix without dendrites but containing dark very small (<1 μm) Si-rich blebs, which are spread in the matrix and locally aligned on the crystal edges of the olivine or chromite grains set into the groundmass (Fig. 7c). The fine-grained olivine crystals in the matrix display a variety of morphologies such as rod, feathery, and dendritic shapes corresponding to the description of hopper olivines (Figs. 3 and 7) by Donaldson et al. (1975). The fourth type of interstitial material seems concentrated along the margin of the whole silicate inclusion, close to the boundary with the metal host.

Based on its composition, the matrix material can be further divided into several subtypes, not corresponding to the petrographic appearances. The composition of the main type of material is quasi-basaltic and contains the highest amount of SiO_2 (Table 2) among the matrix materials in the silicate inclusion. A second type of material is SiO_2 poor and enriched in P_2O_5, CaO, and FeO (CaO and FeO are enriched by about 30% compared to the quasi-basaltic material and the concentration of P_2O_5 quadruples that in the quasi-basaltic material) while a third type is SiO_2 and CaO poor and enriched in P_2O_5, FeO, and MgO (FeO is enriched by about 50%, the concentration of P_2O_5 and MgO are 2.5 and 6 times higher and CaO 6 times lower compared to the quasi-basaltic material) (Table 2). These different types of matrix material are not homogeneously distributed in the inclusion. The quasi-basaltic type is mainly present in the inner part of the inclusion while the two types of SiO_2 poor matrix are mainly present at the edge of the inclusion. Within the SiO_2 and CaO poor matrix area, euhedral chromite crystals are present (Fig. 3a).

Opaque Phases in the Silicate Inclusions

Opaque phases in Netschaëvo silicate inclusions are Fe-Ni metal, troilite, and (Mg-)chromite with kamacite and taenite being the most abundant. These phases are mainly present as large, 100 μm to 1 mm sized irregular grains randomly spread throughout the inclusion (Fig. 8a). Locally they contain troilite inclusions of up to a few tens of μm.

Fe-Ni metal is also present as round and irregular globules a few μm to about 60 μm in diameter. They generally consist of rounded metal blebs (5–20 μm) surrounded by metal dendrites (1–5 μm), with an interstitial P-rich and S-rich phase (Figs. 8b–d). These globules are present in the glassy-like material and between and within olivine and pyroxene crystals. Different petrographic forms of these globules exist and the margins between the P-rich and S-rich phases is always smooth and the shape amoeboid. The majority of the smallest globules (up to 10 μm) consist of metal with inclusions of troilite but troilite crystals with metal inclusions are present as well. Troilite is exclusively present in these assemblages and does not exist as isolated grains. Larger globules range from (sub) rounded to irregular shapes and consist of intergrowths of metal, with a P-rich and S-rich phase (Figs. 8c and 8d). Some of them are dominated by metal and the P-rich phase (Fig. 9).

(Mg-)Chromite is the least abundant phase in the silicate inclusions and concentrated at the contact with the metal host. Generally, the 10 μm to 100 μm sized chromites occur as single grains, surrounded by matrix

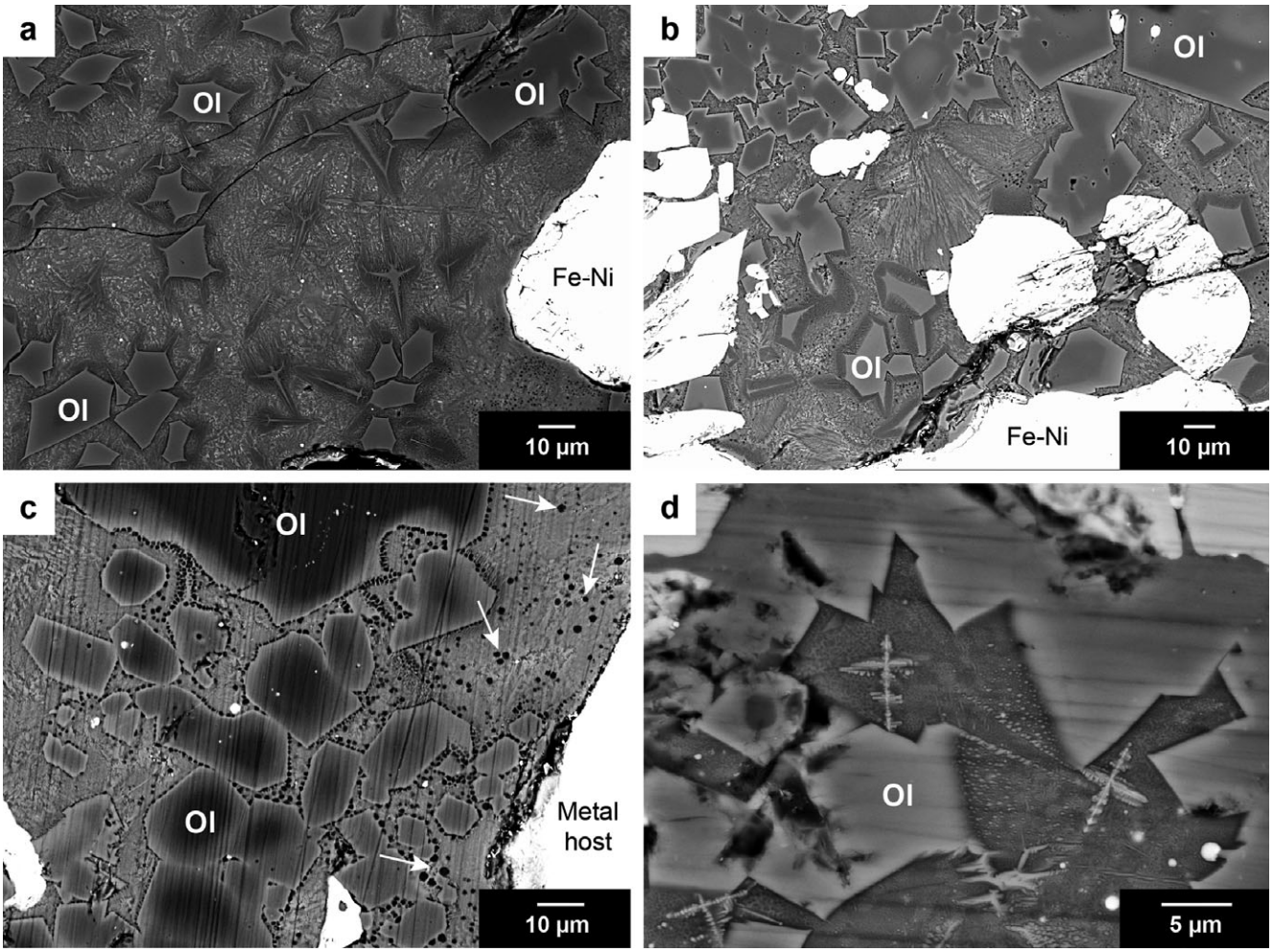

Fig. 7. Backscattered electron images showing the petrographic features of matrix material in the silicate inclusions in Netschaëvo. a) Baby swallowtail olivines embedded in interstitial material consisting of closely packed dendrite-like crystals of olivine set into a glassy appearing matrix. b) Baby swallowtail and compositionally zoned hypidiomorphic olivines with interstitial material. c) Compositionally zoned olivine grains and surrounding interstitial material. Tiny, 0.5—1 μm sized rounded Si-rich droplets are found randomly distributed within the glassy-like material and aligned along the crystal faces of olivine (arrows). d) Glassy-like material with small metal spherules and olivine crystals with overgrowth and branching textures.

material and fine-grained euhedral olivine crystals but locally small inclusions of chromite occur in olivine (Fig. 8b). One large chromite grain of about 300 μm is present, and, in contrast to the other chromite crystals, is irregular in shape. Chromite grains are compositionally homogeneous (Table 1) and do not display any zoning.

DISCUSSION

A Comparison Between the Different Lithologies Present in the Silicate Inclusions of Netschaëvo

In the past, silicate inclusions of Netschaëvo have been described as primitive chondrule-bearing material (Olsen and Jarosewich 1971; Bild and Wasson 1977; Rubin 1990). Olsen and Jarosewich (1971) described the petrographic texture as similar to equilibrated H chondrites and report homogeneous silicate compositions. They reported modal abundances of 52% bronzite, 26% olivine, 5.4% calcic pyroxene, 13.6% plagioclase, 0.9% chromite, 1.6% whitlockite, and 0.5% graphite. A similar description is given by Bogard et al. (2000), who reported recrystallized chondrules and a mineralogy that is roughly chondritic. The shock stage of these silicate inclusions is S2–S3 (Bogard et al. 2000).

Our analyses of the two examined samples of Netschaëvo show different characteristics of the silicate inclusions than in the chondrule-bearing material of Netschaëvo previously described (Olsen and Jarosewich 1971). They are listed below.

Table 2. Average composition and standard deviation (2σ) of the matrix material in Netschaëvo (wt%) determined by electron microprobe analysis.

	SiO_2 rich	SiO_2 poor	SiO_2 and CaO poor
SiO_2	53.4 ± 4.5	36.2 ± 3.0	40.7 ± 5.9
TiO_2	0.4 ± 0.1	0.3 ± 0.1	0.1 ± 0.05
Al_2O_3	7.6 ± 0.9	4.5 ± 1.1	3.3 ± 1.9
Cr_2O_3	0.2 ± 0.1	0.7 ± 0.3	0.5 ± 0.2
FeO	16.9 ± 2.9	21.9 ± 1.9	26.0 ± 1.9
MnO	0.3 ± 0.1	0.3 ± 0.04	0.3 ± 0.04
MgO	3.9 ± 1.3	7.2 ± 2.8	18.3 ± 7.8
CaO	10.6 ± 2.6	14.2 ± 3.0	1.7 ± 1.6
Na_2O	2.1 ± 0.6	1.1 ± 0.3	0.5 ± 0.5
K_2O	0.3 ± 0.2	0.2 ± 0.04	0.1 ± 0.1
P_2O_5	3.0 ± 2.0	12.1 ± 2.2	8.0 ± 0.7
NiO	0.0	0.1 ± 0.04	0.04 ± 0.02
Cl	1.3 ± 0.3	1.9 ± 0.4	0.2 ± 0.2
Total	99.7	100.3	99.7
No. of analyses	10	12	4

1. In the chondrule-bearing inclusions the olivine and pyroxene grains have a homogeneous composition while the rims of these minerals, and the fine-grained olivines, show a wide range of compositions. This, together with their crystal shape, suggests formation during very fast crystallization from a melt. The concentration of minor elements in these rims and grains, for example, the concentrations of CaO and Cr_2O_3 in the newly crystallized olivines, are higher than those observed in equilibrated chondrites and is commonly related to shock-melted ordinary chondrites (McCoy et al. 1991).
2. The matrix of the investigated samples contains fine-grained glassy-like material without crystals, based on the examination under SEM. This material probably did not crystallize due to fast cooling. In the chondrule-bearing inclusions, there is no glassy matrix as everything is crystalline.
3. The presence of melts of different composition unevenly distributed in the inclusions indicates instantaneous melting and crystallization without re-equilibration or homogenization of the melt and crystals afterward.
4. Although Ca-pyroxene is present in the chondrule-bearing clasts of Netschaëvo (Olsen and Jarosewich 1971), this phase is not present in the examined samples. This probably can be explained by the fact that this phase completely melted (due to its lower melting point compared to olivine and low-Ca pyroxene; see the Cooling History section) and contributed to the fine-grained matrix material, as a consequence of heating and melting.
5. The intergrowths present in both host and globules in the metal matrix of the silicate inclusions in the investigated samples show similarities with features produced in three phase experiments conducted by Chabot and Drake (2000). In these experiments, mixtures of dominantly Fe, Ni, FeS, and P were heated up to temperatures ranging from 1050 to 1400 °C and quenched in water afterward. Three phases were present in all experiments (1) solid metal, (2) a P-rich metallic liquid, and (3) a S-rich metallic liquid forming a dendritic texture. The experiments showed that the P-rich and S-rich metallic phases did not quench to a single homogenous phase but instead formed Fe-dendrites surrounded by interstitial P-rich and S-rich phases. Similar dendritic textures are also observed in the iron meteorite Silver Crown in a completely molten and rapidly solidified schreibersite particle (Buchwald 1975) and in the metal–troilite intergrowths of the Mundrabilla IAB-ungrouped meteorite (Scott 1982). The presence of these quenched features in Netschaëvo metal indicate that melting and rapid cooling took place in the metal host, as well as the silicate inclusions. In comparison, the metal host of the chondrule-bearing clasts displays medium-sized Widmanstätten pattern with kamacite lamellae 1.25 ± 0.35 mm in width (Buchwald 1975).
6. The large taenite grains present in the silicate inclusions of Netschaëvo contain a higher amount of P (0.19 wt%) than observed for taenite in equilibrated ordinary chondrites (< 0.10 wt%; Smith and Goldstein 1977). The enrichment of P in metal in chondrites is interpreted as a result of shock metamorphism and is probably produced by the dissolution of P in metal as a consequence of reduction of phosphates at high temperatures (Taylor and Heymann 1971; Smith and Goldstein 1977). This scenario is likely for Netschaëvo as well.
7. The two examined samples have silicate inclusions that show strong similarities with textures observed in the Martian shergottites Yamato 980459 (Greshake et al. 2004) and ALH-77005 shergottite (Ikeda 1994) as well as in several chondritic impact-melt rocks and regolith breccias (Taylor et al. 1979; Casanova et al. 1990; Nakamura et al. 1990; Bogard et al. 1995; Yamaguchi et al. 1999; Mittlefehldt and Lindstrom 2001; Folco et al. 2002, 2004; Norman and Mittlefehldt 2002; Rubin 2002; Burbine et al. 2003; Rubin and Jones 2003; Grier et al. 2004; Bischoff et al. 2011; Metzler et al. 2011).

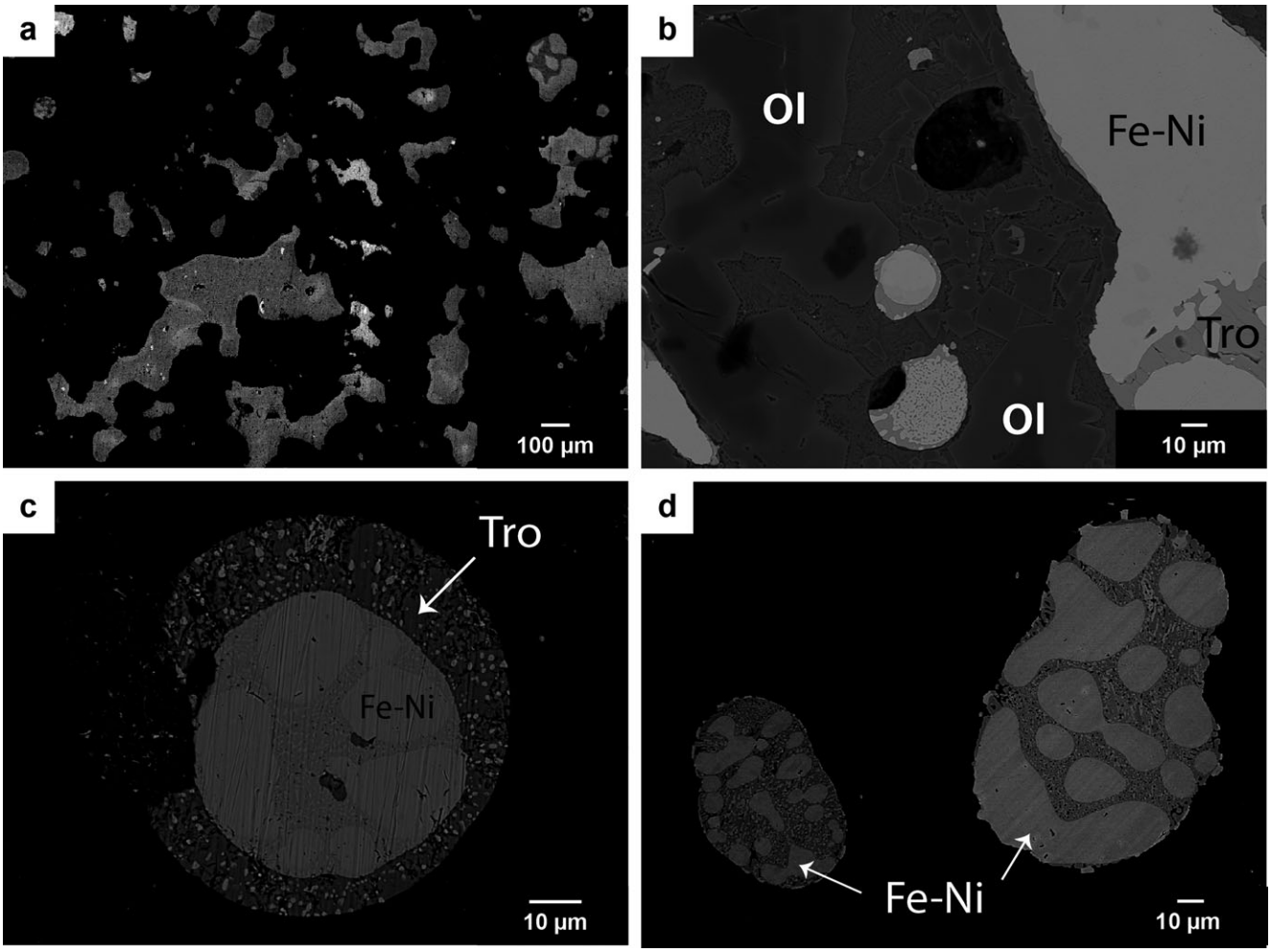

Fig. 8. Backscattered electron images showing the petrographic features of opaque phases in Netschaëvo. a) Overview of the distribution of opaque phases showing the large irregular grains and the smaller (sub) rounded globules. b) Metal spheres spread in the silicate material. They consist of a mixture of metal (white) and troilite (light gray). c) Metal spherule whose interior consists of Fe-Ni (white) with a P-rich phase (light gray), and whose rim consists of troilite (dark gray) with inclusions of metal (white). d) Spherules consisting of an intergrowth of metal, a P-rich and a S-rich phase (elemental mapping of left spherule is shown in Fig. 9).

These features, considered both individually and all together, strongly suggest that the investigated samples experienced melting to a certain extent. Furthermore, the similarity of textures between meteorites that show impact melts and the above-mentioned features likely indicates that the investigated silicate inclusions contain impact melt. The investigated pieces can, thus, be classified as impact-melt rocks (IMR) (Bischoff et al. 2006; Stöffler and Grieve 2007), constituting the first occurrence of impact melt in IIE iron meteorites.

In the silicate inclusions investigated in this study, the composition of the cores of coarse-grained olivine ($Fa_{14.3 \pm 0.3}$) and low-Ca pyroxene ($Fs_{14.8 \pm 0.3}$) is almost identical to the olivine and pyroxene compositions ($Fa_{14.1}$ and $Fs_{13.6}$) in the chondrule-bearing pieces of Netschaëvo reported by Mittlefehldt et al. (1998) (Fig. 10). Also the concentration of Co and Ni in kamacite (3.6–4.8 and 64.4–83.9 mg g^{-1}, respectively) in the silicate inclusions correspond well with the mean Co and Ni content (4.3 and 86 mg g^{-1}, respectively) reported by Bild and Wasson (1977) for the chondrule-bearing inclusions of Netschaëvo. The fact that the compositions of olivine and pyroxene match well indicate that the investigated silicate inclusions likely originate from the same precursor material as the chondrule-bearing clasts. The fact that the investigated samples are impact-melt rocks strongly suggests that they are produced by impact melting of the same original material forming the chondrule-bearing clasts of Netschaëvo at the surface of the parent body.

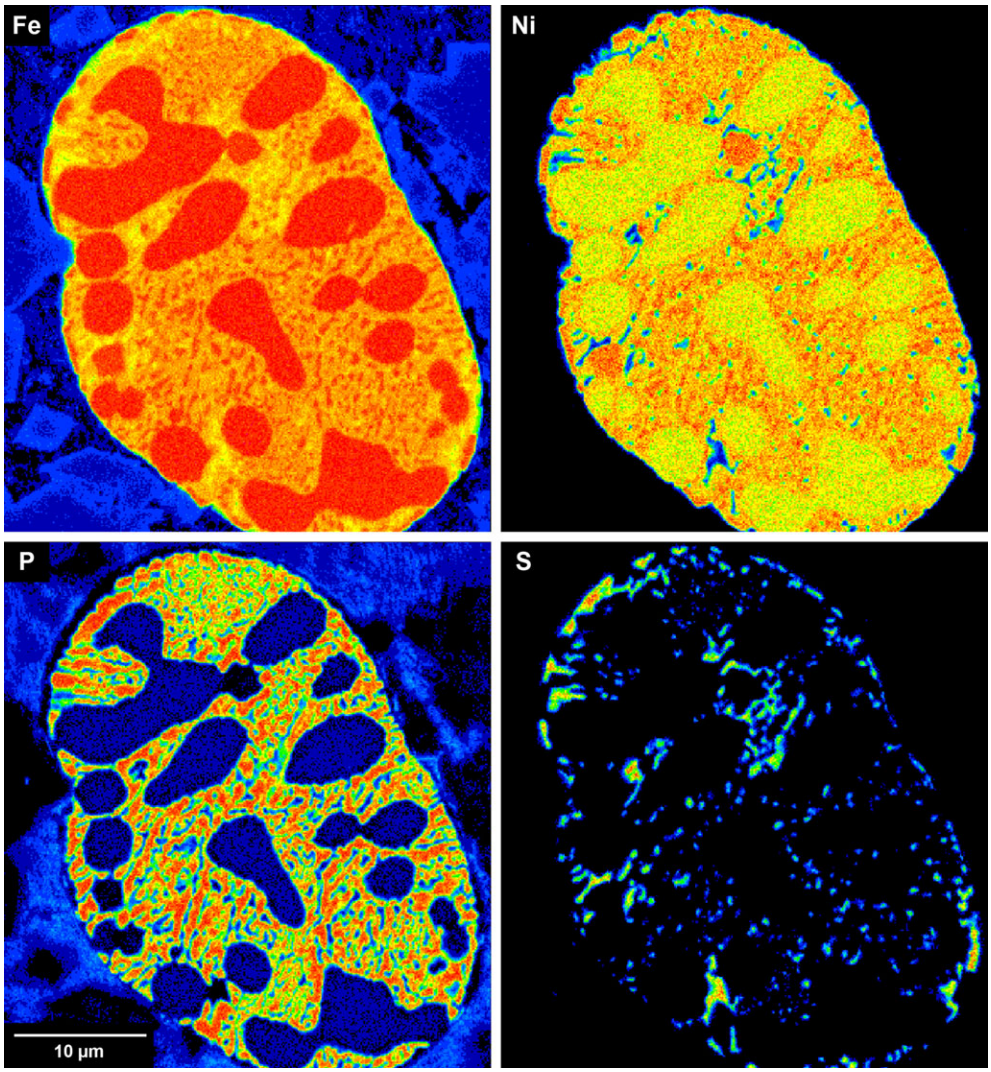

Fig. 9. X-ray elemental mapping of Fe, P, S, and Ni in a metal spherule in the investigated silicate inclusion of Netschaëvo (the BSE-image of the spherule is shown in Fig. 8d). Relative X-rays intensities range from low (blue-green) to high (yellow – orange – red).

Cooling History

As the investigated silicate inclusions are believed to be the product of impact melting, their precursor material experienced rapid heating. This indicates that melting did not occur in equilibrium at the eutectic and that the individual melting points of the minerals need to be considered to constrain the melt peak temperature of the inclusions. The melting temperatures of the minerals present in the original chondrule-bearing material of Netschaëvo are 1850 °C for olivine with a composition of $Fa_{14.3 \pm 0.3}$ (Bowen and Schairer 1935), 1550 °C for low-Ca pyroxene with a composition of $Fs_{14.7 \pm 0.1}$ (Huebner and Turnock 1980), 1350 °C (Deer et al. 1992) for calcic pyroxene (89% diopside; Olsen and Jarosewich 1971), 1300 °C (Deer et al. 1992) for albitic plagioclase ($Ab_{82}An_{14}Or_4$; Olsen and Jarosewich 1971), and 1390 °C (Irving et al. 2011) for merrillite. The fact that only the cores of coarse-grained mafic grains are preserved in the silicate inclusions indicate that the majority of smaller olivine and pyroxene grains have been completely molten. Based on this information, the peak temperature must have likely reached 1850 °C, as a large fraction of the olivine grains was molten. However, impact melting is not only controlled by the melting temperature of individual minerals. Also shock impedance, the shock wave velocity multiplied by the mineral's density, plays an important role. For chondrites, the two extremes are metal, a high-impedance phase and albite, a low-impedance phase (Sharp and DeCarli 2006). This means that localized stress and temperature will be the highest

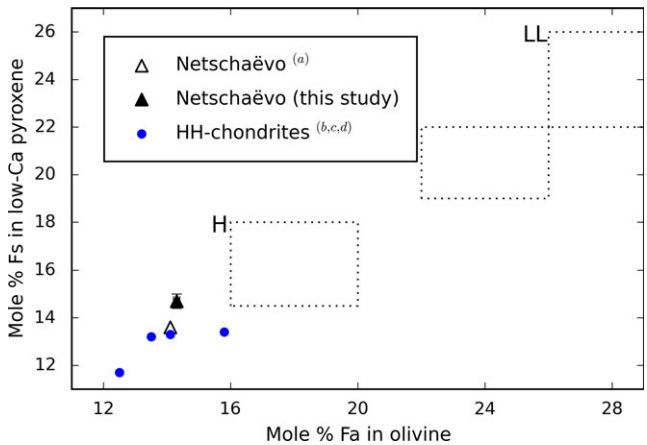

Fig. 10. Fs versus Fa molar contents of the cores of the relict olivines and pyroxenes in this study compared with those of previously examined silicate inclusions of Netschaëvo, HH, H, L, and LL chondrites. Data from: [a]Mittlefehldt et al. (1998), [b,c,d]Scott et al. (1985); Whitlock et al. (1991), Russell et al. (1998); and for H, L, and LL chondrites from Brearley and Jones (1998).

at the metal–silicate interfaces (Stöffler et al. 1991). Another factor that needs to be considered is the mineral grain size. Logically, the smaller grains will be affected by the sudden increase in temperature preferentially, while larger grains can resist longer and thus have a higher probability to be preserved. All these factors taken into account resulted in the preferential and complete melting of calcic pyroxene, plagioclase, and merrillite, while low-Ca pyroxene and olivine, the dominant minerals in the inclusion, were partly preserved. This is consistent with disequilibrium partial melting experiments conducted on an L chondrite by Feldstein et al. (2001) who observed that clinopyroxene, plagioclase, and phosphate are the first phases to melt. Although this melting sequence is also observed in equilibrium melting, the history of the Netschaëvo meteorite and the observed quenching textures support the hypothesis of impact melting in this case.

The cooling rate of the investigated lithology can be roughly evaluated by the characteristic morphologies of the fine-grained and dendrite-like olivine crystals. Several studies have focused on the classification and formation of olivine morphologies and the experimental reproduction of these features (Donaldson et al. 1975; Lofgren 1989; Faure et al. 2003, 2007). Faure et al. (2003) classified all the different olivine morphologies reported in the literature into four groups (polyhedral, tabular, hopper, dendrites), related to the growth conditions. Based on experimental results, the presence of these morphologies can be used to constrain the cooling history of the melt. Experiments by Donaldson et al. (1975) have shown that the presence of polyhedral forms points to a cooling rate of about 0.5 °C h^{-1}. According to the experiments of Faure et al. (2003), cooling rates up to 2 °C h^{-1} always produce uniquely polyhedral forms, independent of the undercooling. With increasing cooling rate, from 47 °C h^{-1} on, polyhedral forms evolve into tabular or hopper forms. From this point on, the morphological evolution depends on the degree of undercooling (Faure et al. 2003). Undercooling in the range of 60–90 °C results in baby swallowtail shapes, while an undercooling of >70–90 °C produces swallowtail crystals. Among the newly crystallized olivines, a variety of morphologies are present in the silicate inclusions of Netschaëvo. The inclusions of Netschaëvo are dominated by hopper forms (Figs. 2d and 3) and dendrites, in particular baby swallowtails, swallowtails, and feathery crystals and contain only minor polyhedral forms (Figs. 2d, 3a, and 3b). Baby swallowtails, swallowtails, and feathery crystals correspond to rapid growth morphologies produced at undercooling rates of 68, 122, and 258 °C, respectively, for a cooling rate of 1890 °C h^{-1}, according to Faure et al. (2003). In other words, as the degree of supercooling increases, more highly branching shapes will be formed (Walton and Herd 2007). Based on these observations and on the experiments of Faure et al. (2003), it is likely that the Netschaëvo silicate inclusions initially experienced a relatively slow cooling (<2 °C h^{-1}), which allowed the formation of the polyhedral crystals, followed by a much higher cooling rate and a high degree of undercooling, as suggested by the occurrence of dendritic shapes. From comparison with the experimental work, the presence of swallowtail olivine indicates that the degree of undercooling in Netschaëvo silicate was likely ca. 122 °C, at a high cooling rate. Also the higher concentration of Cr_2O_3 in the newly crystallized olivine grains is a consequence of rapid cooling that prevented crystallization of chromite inclusions. Although we can roughly evaluate the cooling rate from the varieties of olivine morphologies, absolute cooling rates cannot be estimated, because olivine crystallization is controlled by the local availability of nuclei (Faure et al. 2003). However, other factors, such as the duration at the peak temperature and the availability of nuclei for crystallization of new olivine, could also have influenced the cooling history.

In the examined impact-melt rock clasts, the rims crystallizing onto the preserved low-Ca pyroxene cores progressively incorporate more Ca, finally leading to the crystallization of pigeonite at their outermost parts (Fig. 4). Pigeonite is only preserved in quenched rocks, because it exsolves augite and afterward inverts to low-Ca pyroxene for slow cooling (Poldervaart and Hess 1951). In our case, pigeonite likely formed as a

metastable phase, as the rock cooled too fast for low-Ca pyroxene and exsolution lamellae to form. The fact that pigeonite occurs in the outer rim of the preserved low-Ca pyroxenes and did not form separate crystals is probably due to degree of undercooling, which did not allow nucleation of individual grains. This phenomenon is also observed in, e.g., the Martian shergottites Yamato 980459 (Greshake et al. 2004). Based on these observations, it can be concluded that the silicate inclusions were quenched after the crystallization of pigeonite. The temperature at which pigeonite crystallizes is around 1100 °C (Poldervaart and Hess 1951). The temperature at which plagioclase with a composition of $Ab_{82}An_{14}Or_4$ crystallizes is about 1140 °C (Deer et al. 1992). This means that if only temperature controls the crystallization path plagioclase should have crystallized as well. As other factors than temperature play a role during crystallization, such as the melt composition, the availability of nuclei, etc., we can only conclude that, in this particular case, pigeonite likely crystallized before plagioclase and that the sample was quenched immediately afterward. The crystallization of phosphate in the P-rich melt located at the outer part of the silicate inclusion was probably inhibited by fast cooling.

The shapes, meniscus-like boundaries and the globule-in-globule forms (Figs. 8b–d) of the metal-phosphor-sulfur intergrowths in the silicate inclusion indicate that these features formed as immiscible liquid phases. Based on the textures, three immiscible phases were probably present, Fe-Ni, Fe-FeS, and Fe-Ni-P. Although metal-troilite globules have been described in chondrites (Scott 1982), the globules containing metal, a P-rich and a S-rich phase, observed in the investigated clasts, have so far not been described in ordinary chondrites. Similar features have been described in lunar samples (Goldstein et al. 1970, 1972; McKay et al. 1973). McKay et al. (1973) have experimentally constrained the conditions at which these features form. In the experiments that produced a quenched Fe-P liquid, the starting material (similar to KREEP basalt) was heated to 1350 °C for 1 h and quenched from 1250 °C. This indicates that fast cooling is necessary to produce the intergrowths observed in the investigated silicate inclusions of Netschaëvo. Rapid cooling is also reflected by the fact that troilite and metal occur as small droplets in the glassy-like material and did not have time to segregate into larger pools. Also the absence of the Widmanstätten pattern in the IMR samples indicate that its growth was inhibited by fast cooling, as the Widmanstätten pattern is developed as a two-phase intergrowth of kamacite and taenite during slow cooling of the parent body (Goldstein et al. 2009).

In many impact-melt rocks, high-pressure polymorphs, such as ringwoodite, are present. Raman analyses have confirmed that no such phases are present in the investigated inclusions of Netschaëvo. One explanation might be that the melt inclusion was too large (a few mm in diameter) and stayed too long at high temperatures, exceeding the shock pulse duration required for the crystallization and preservation of high-pressure polymorphs (Shaw and Walton 2013).

Summarizing, the chemical and mineralogical characteristics of the silicate inclusions as well as of the metal host, such as the hopper morphology of the newly crystallized grains, the zoning in olivine and pyroxene, the presence of pigeonite, the occurrence of glassy-like material, the globules and intergrowths in the metal host, indicate that the investigated sample underwent fast cooling and nonequilibrium crystallization.

Silicate Liquid Immiscibility

The composition and the spatial distribution of the several types of melt in Netschaëvo silicate can be explained in the framework of silicate liquid immiscibility. Although an alternative explanation is that melting occurred only locally, with the composition of the melt controlled by the mineral assemblage surrounding it, this scenario seems unlikely. A random distribution of the different kinds of melts throughout the inclusion would be expected, and this is not the case, as the quasi-basaltic melt is concentrated in the inner part of the silicate inclusions, while SiO_2 poor melt is concentrated at the outer part of the inclusion. The most likely scenario assumes that the melt pockets were mobilized and well mixed throughout the inclusion, and that due to silicate liquid immiscibility several types of melts were formed. A similar process was reported by Kamenetsky et al. (2013) who observed a light (L_{Fe}) SiO_2 poor melt, enriched in P_2O_5, FeO, MgO, and CaO, and a dark SiO_2 rich melt (L_{Si}), enriched in Al_2O_3, Na_2O, and K_2O in silicate melts entrapped by native iron in an intrusive body of tholeiitic gabbro in the Siberian large igneous province. This is the case for Netschaëvo, where the SiO_2 poor melt is situated at the border with the metal host, the L_{Fe} is present as a rim in the silicate pool, in contact with the native iron (Kamenetsky et al. 2013). The immiscibility of two liquids, one rich in Fe, P, Ti, Mg, Mn, and Ca, and one rich in elements such as Si, Al, and alkalis, has been observed in several experiments and rocks (Watson 1976; Freestone 1978; Roedder 1978, 1979; Ryerson and Hess 1978; Visser and Koster van Groose 1979) and probably also took place in the silicate inclusions of Colomera IIE and Sombrerete (ungrouped) to form P-rich segregations (Ruzicka et al. 2006).

Formation of Netschaëvo

Two different silicic lithologies, chondrule-bearing silicate inclusions and the investigated IMR clasts, are present in Netschaëvo. The formation conditions for these two lithologies are very different. According to Bogard et al. (2000), the chondrule-bearing clasts have a shock stage of S2–S3, corresponding to a shock pressure of 15–20 GPa (Stöffler et al. 1991). Temperatures in the chondrule-bearing clasts must have been at least 750–950 °C (Dodd 1981), based on the fact that textures are corresponding to petrologic type 6, or even higher, according to Ruzicka (2014), who classifies the Netschaëvo silicate inclusions as a type 7. Slow cooling is also necessary to produce these coarse-grained type 6–7 equilibrated textures. Shock pressures for the IMR clasts on the other hand, must have been at least 75–90 GPa (Stöffler et al. 1991) and temperatures probably reached roughly 1850 °C based on the melting temperature of the individual minerals (see the Cooling History section). Stöffler et al. (1991) defined a temperature range of 1500–1750 °C for impact-melt rocks. It is difficult to evaluate the exact temperature range, as the temperature that is reached strongly depends on the peak shock pressure, the mineralogy and porosity of the material (Stöffler et al. 1991). Taking this into account, the temperature in the IMR clasts must have been high, probably between 1500 and 1800 °C. Cooling was very quick, at a possible cooling rate of about 1890 °C h^{-1}, as argued earlier. The observation of the presence of these two lithologies indicates that the Netschaëvo iron meteorite is a breccia containing metamorphosed and impact-melt rock (IMR) clasts.

Radiometric dating ($^{40}Ar/^{39}Ar$) on a previously examined chondrule-bearing silicate inclusion of Netschaëvo yields an age of 3.79 ± 0.03 Ga (Niemeyer 1980). It is assumed that the age of Netschaëvo has been reset in a late impact event (Bogard et al. 2000; Ruzicka 2014). Although no radiometric dating has been performed on the IMR clasts, we can reasonably assume that this impact event was responsible for the formation of the IMR clasts that were situated at the surface of the impacted body. The question arises then if the impact was also responsible for the thermal metamorphism observed in the chondrule-bearing clast. Two possible scenarios need to be considered. In the first one thermal metamorphism caused by the decay of short-lived nuclides took place when the chondritic parent body was formed, in the beginning of the solar system. Then, around 3.79 ± 0.03 Ga an impact occurred, melting some of the metamorphosed material to create the IMR clasts, while other metamorphosed material was not affected by the impact. A second option would be that the impact is responsible for the formation of the IMR clasts and the metamorphosed clasts, due to postimpact burial and annealing. This event could be reflected in the slow cooling rate (~3 °C Ma^{-1}) of the metamorphosed chondritic material defined by Rubin (1990). However, this second scenario seems unlikely. Textures present in type 6–7 chondrites require very slow cooling, as determined by Rubin (1990) and this cannot be reconciled with the fast cooling experienced by the IMR clasts, as both types of lithology are included in the same meteorite. Even if slow cooling occurred after the impact, this should also have been recorded in the IMR clasts, and they do not show any evidence of re-equilibration or annealing. The slow cooling rate defined by Rubin (1990) probably reflects thermal metamorphism caused by decay of short-lived radionuclides in the beginning of the solar system. The cooling rate is comparable to that defined for thermal metamorphism in ordinary chondrites. For example, the cooling rate of Estacado H6 chondrite is estimated to be between 2 and 13 °C Ma^{-1} (Blinova et al. 2007), and Scott et al. (2014) estimated an average cooling rate of 10–50 °C Ma^{-1} based on 30 H chondrites. At the time of impact, around 3.79 ± 0.03 Ga, the parent body was cold, as no heat from radioactive decay was left. This means that the cooling rate should be determined by deep burial of the material. Davison et al. (2012) studies the postimpact thermal histories of parent bodies by simulating a range of impact scenarios. They concluded that an impact with a collision velocity of 4 km s^{-1} between a parent body of 250 km with a high porosity and an impactor of 25 km can bury material at depth with cooling rates at 773 K of typically 1–1000 K Ma^{-1}, resulting in the production of type 6 material. Scott et al. (2014) investigated this issue based on the cooling rates of 30 H chondrites. They found that regolith breccias cooled at rates of 5–100 °C Ma^{-1}, which is in the same range of all other chondrites. As the investigated regolith breccias contained cloudy taenite and other features of metal in unshocked chondrites, the measured cooling rates were pristine and not affected by the impact event. These cooling rates thus indicate that impact did not cause metamorphism. Another observation confirming this hypothesis is the near absence of slowly cooled meteorites with Ar-Ar ages under 4 Ga (Scott et al. 2014).

Therefore, indigenous metamorphism probably took place at the time of the formation of the Netschaëvo parent body, when radioactive decay was still active. If the impact was not responsible for the thermal metamorphism experienced by the Netschaëvo chondrule-bearing clasts then thermal metamorphism could also not have been responsible for the resetting of

the Ar-Ar age, as suggested by Ruzicka (2014). It is likely that the chondrule-bearing clasts experienced a peak temperature, caused by the impact event, high enough to reset the Ar-Ar age, but not to significantly affect the mineral assemblage. The shock stage observed in these inclusions of Netschaëvo (S2–S3; Bogard et al. 2000) is also proof of this later impact event.

An impact occurring around 3.79 ± 0.03 Ga (Niemeyer 1980) implies that the target material was cold, as heating mechanisms such as radioactive decay were no longer active (Kleine et al. 2005). As the impact occurred on a cold target, brittle deformation must have taken place, and indeed this is supported by the angular shape of the chondrule-bearing silicate clasts of Netschaëvo (Rubin 1990). This is also supported by the fact that metal and troilite did not form a veining network in the IMR silicate clasts, as would be expected for a body that is still hot, as observed in Portales Valley (Ruzicka et al. 2005).

Implications for IIE Group

Netschaëvo, together with Kodaikanal and Watson, belongs to the young IIE group (average age = 3.60 ± 0.15 Ga; Ruzicka 2014). Bogard et al. (2000) suggested that these young ages were the result of resetting the isotopic systems in a common impact event with an age of 3.676 Ga. Evidence for this event has been recorded in petrographic features in these meteorites, such as the local distortion of the Widmanstätten texture for Kodaikanal and Watson (Bence and Burnett 1969; Olsen et al. 1994). Ruzicka (2014) states that the silicate inclusion of Watson is what is expected to be the product of an impact melting process. This hypothesis is based on analyses performed by Olsen et al. (1994) that indicate that the metal and sulfide have been removed from the silicate by melting, and that no significant fractionation of silicates took place as proven by the flat REE bulk pattern. Based on the evidence for metal–silicate separation during shock melting in chondrites (Tomkins et al. 2013), Ruzicka (2014) assumes that metal has been removed from the silicate inclusion and added to the host as a result of a collision.

Netschaëvo, on the other hand, could fit into the endogenic-only formation model from the standpoint of thermal histories, silicate nature, and metal concentration, according to Ruzicka (2014). The main argument is based on the fact that the silicate inclusions in Netschaëvo correspond to type 7 (Ruzicka 2014), indicating they have been slowly heated under high-grade metamorphism, with temperatures that were higher than those experienced by type 6 chondrites. Under these conditions, melting of silicates was prevented and metal and sulfide did not significantly separate from the silicate material. The fact that we found impact-melt rocks of Netschaëvo strongly suggests that this meteorite has formed by a collision, and not by endogenic heating, although endogenic heating likely occurred on the parent body. This strengthens the hypothesis that an impact event occurred around 3.6–3.7 Ga that was recorded in all young IIE, indicating that they probably originated on the same parent body in a common impact event, as already suggested by Bogard et al. (2000).

CONCLUSIONS

A detailed petrographic examination of all textures observed in two samples of Netschaëvo IIE indicate that these pieces consist of impact melt that underwent rapid cooling, undercooling, and fast crystallization, resulting in the presence of quenched material, in the silicate inclusions as well as in the metal host. The investigated pieces of Netschaëvo can be classified as impact-melt rocks (IMR) and do not correspond to the previously described silicate material of Netschaëvo that are chondrule-bearing chondritic clasts. Coarse-grained olivine and pyroxene in the IMR clasts display core compositions ($Fa_{14.3 \pm 0.3}$ and $Fs_{14.8 \pm 0.5}$) that are consistent with those in the chondrule-bearing clasts ($Fa_{14.1}$ and $Fs_{13.6}$), and hence were likely preserved from melting. We therefore conclude that the precursor material of the IMR and the chondrule-bearing clasts originated from the same parent body. The occurrence of both lithologies in the same meteorite suggests that Netschaëvo itself is a breccia containing metamorphosed and IMR clasts. This strengthens the hypothesis that all young IIE originated in a common impact event and that impact played a major role in the formation of this group.

Acknowledgments—The authors thank the Museum für Naturkunde, Berlin, Germany, and the Natural History Museum, London, United Kingdom, for providing the samples. We also thank Priya Laha, Peter Czaja, and Kitty Baert for their technical support on the SEM, EMPA, and Raman spectroscopy, respectively. NVR thanks Lutz Hecht for his assistance with the EMPA. Editorial handling by Gretchen Benedix and reviews by Alan Rubin, Alex Ruzicka, and Addi Bischoff are gratefully acknowledged. NVR and VD thank the FRS-FNRS for funding through an incentive grant. VD also thanks the ERC StG "ISoSyC" for present support. LP, VD, and PhC thank the Belgian Science Policy Office (BELSPO). PhC thanks the Research Foundation Flanders (FWO; grants: G.A078.11 & G.0021.11). This research has been partly funded by the Interuniversity

Attraction Poles Programme "Planet Topers" initiated by BELSPO.

Editorial Handling—Dr. Gretchen Benedix

REFERENCES

Armstrong J. T., Kennedy A. K., Carpenter P. K., and Albee A. L. 1990. Petrography and trace element chemistry of Colomera (IIE) silicate inclusions: Rhyolitic plums in the pudding. Proceedings, 21st Lunar and Planetary Science Conference. pp. 22–23.

Bence A. E. and Burnett D. S. 1969. Chemistry and mineralogy of the silicates and metal of the Kodaikanal meteorite. *Geochimica et Cosmochimica Acta* 33:387–407.

Bild R. W. and Wasson J. T. 1977. Netschaëvo: A new class of chondritic meteorite. *Science* 197:58–62.

Bischoff A., Scott E. R., Metzler K., and Goodrich C. A. 2006. Nature and origins of meteoritic breccias. In *Meteorites and the early solar system II*, edited by Lauretta D. S., and McSween H. Y.. Tucson, Arizona: The University of Arizona Press. pp. 679–712.

Bischoff A., Vogel N., and Roszjar J. 2011. The Rumuruti chondrite group. *Chemie der Erde—Geochemistry* 71:101–133.

Blinova A., Amelin Y., and Samson C. 2007. Constraints on the cooling history of the H-chondrite parent body from phosphate and chondrule Pb-isotopic dates from Estacado. *Meteoritics & Planetary Science* 42:1337–1350.

Bogard D. D., Garrison D. H., Norman M., Scott E. R. D., and Keil K. 1995. ^{39}Ar-^{40}Ar age and petrology of Chico: Large scale impact melting on the L chondrite parent body. *Geochimica et Cosmochimica Acta* 59:1383–1399.

Bogard D. D., Garrison D. H., and McCoy T. J. 2000. Chronology and petrology of silicates from IIE iron meteorites: Evidence of a complex parent body evolution. *Geochimica et Cosmochimica Acta* 64:2133–2154.

Bowen N. L. and Schairer J. F. 1935. The system MgO – FeO – SiO_2. *American Journal of Science* 29:151–217.

Brearley A. J. and Jones R. H. 1998. Chondritic meteorites. In *Planetary materials*, edited by Papike J. J. Albuquerque, New Mexico: Mineralogical Society of America. pp. 3.1–3.191.

Buchwald V. F. 1975. *Handbook of iron meteorites*. Berkeley: University of California Press 1418 p.

Bunch T. E. and Olsen E. 1968. Potassium feldspar in Weekeroo Station, Kodaikanal, and Colomera iron meteorites. *Science* 160:1223–1225.

Bunch T. E., Keil K., and Olsen E. 1970. Mineralogy and petrology of silicate inclusions in iron meteorites. *Contributions to Mineralogy and Petrology* 25:297–340.

Burbine T. H., Folco L., Capitani G., Bland P. A., Menvies O. N., and McCoy T. J. 2003. Identification of nanophase iron in a H chondrite impact melt (abstract #5209). *Meteoritics & Planetary Science* 38:A111.

Burnett D. S. and Wasserburg G. J. 1967. Evidence for the formation of an iron meteorite at 3.8×10^9 years. *Earth and Planetary Science Letters* 2:137–147.

Casanova I., Keil K., Wieler R., San Miguel A., and King E. A. 1990. Origin and history of chondrite regolith, fragmental and impact-melt breccias from Spain. *Meteoritics* 25:127–135.

Casanova I., Graf T., and Marti K. 1995. Discovery of an unmelted H-chondrite Inclusion in an iron meteorite. *Science* 268:540–542.

Chabot N. L. and Drake M. J. 2000. Crystallization of magmatic iron meteorites: The effects of phosphoros and liquid immiscibility. *Meteoritics & Planetary Science* 35:807–816.

Choi B.-G., Ouyang X., and Wasson J. T. 1995. Classification and origin of IAB and IIICD iron meteorites. *Geochimica et Cosmochimica Acta* 59:593–612.

Clayton R. and Mayeda T. 1996. Oxygen isotope studies of achondrites. *Geochimica et Cosmochimica Acta* 60:1999–2017.

Davison T. M., Ciesla F. J., and Collins G. S. 2012. Post-impact thermal evolution of porous planetesimals. *Geochimica et Cosmochimica Acta* 95:252–269.

Deer W. A., Howie R. A., and Zussman J. 1992. *Rock-forming minerals*, 2nd ed. Hong Kong: Longman Scientific & Technical. 696 p.

Dodd R. T. 1981. *Meteorites: A petrologic-chemical synthesis*. Cambridge, UK: Cambridge University Press. 368 p.

Donaldson C. H., Usselman T. M., Williams R. J., and Lofgren G. E. 1975. Experimental modeling of the cooling history of Apollo 12 olivine basalts. Proceedings, 6th Lunar and Planetary Science Conference. pp. 843–869.

Faure F., Trolliard G., Nicollet C., and Montel J.-M. 2003. A developmental model of olivine morphology as a function of the cooling rate and the degree of undercooling. *Contributions to Mineralogy and Petrology* 145:251–263.

Faure F., Schiano P., Troilliard G., Nicollet C., and Soulestin B. 2007. Textural evolution of polyhedral olivine experiencing rapid cooling rates. *Contributions to Mineralogy and Petrology* 153:405–416.

Feldstein S. N., Jones R. H., and Papike J. J. 2001. Disequilibrium partial melting experiments on the Leedey L6 chondrite: Textural controls on melting processes. *Meteoritics & Planetary Science* 36:1421–1441.

Folco L., Bland P. A., D'Orazio M., Franchi I. A., and Rocchi S. 2002. Dar al Gani 896: A unique picritic achondrite (abstract #5176). *Meteoritics & Planetary Science* 39:A49.

Folco L., Bland P. A., D'Orazio M., Franchi I. A., Kelley S., and Rocchi S. 2004. Extensive impact melting on the H-chondrite parent asteroid during the cataclysmic bombardment of the early solar system: Evidence from the achondritic meteorite Dar al Gani 896. *Geochimica et Cosmochimica Acta* 68:2379–2397.

Freestone I. C. 1978. Liquid immiscibility in alkali-rich magmas. *Chemical Geology* 23:115–123.

Goldstein J. I., Henderson E. P., and Yakowitz H. 1970. Investigation of lunar metal particles. Proceedings, Apollo 11 Lunar Science Conference. pp. 177–191.

Goldstein J. I., Axon H. J., and Yen C. F. 1972. Metallic particles in the Apollo 14 Lunar soil. Proceediongs, 3rd Lunar Science Conference. pp. 1037–1064.

Goldstein J. I., Scott E. R. D., and Chabot N. L. 2009. Iron meteorites: Crystallization, thermal history, parent bodies, and origin. *Chemie der Erde* 69:293–325.

Greshake A., Fritz J., and Stöffler D. 2004. Petrology and shock metamorphism of the olivine-phyric shergottite Yamato 980459: Evidence for a two-stage cooling and a single-stage ejection history. *Geochimica et Cosmochimica Acta* 68:2359–2377.

Grier J. A., Kring D. A., Swindle T. D., Rivkin A. S., Cohen B. A., and Britt D. T. 2004. Analyses of the chondritic meteorite Orvinio (H6): Insight into the origin and evolution of shocked H chondrite material. *Meteoritics & Planetary Science* 39:1475–1493.

Heilbronner R. 2000. Automatic grain boundary detection and grain size analysis using polarization micrographs or orientation images. *Journal of Structural Geology* 22:969–981.

Hsu W. 2003. Rare earth element geochemistry and petrogenesis of Miles (IIE) silicate inclusions. *Geochimica et Cosmochimica Acta* 67:4807–4821.

Huebner J. S. and Turnock A. C. 1980. The melting relations at 1 bar of pyroxenes composed largely of Ca-, Mg-, and Fe-bearing components. *American Mineralogist* 65:225–271.

Ikeda Y. 1994. Petrography and petrology of the ALH-77005 shergottite. Proceedings, 7th NIPR symposium. pp. 9–29.

Ikeda Y. and Prinz M. 1996. Petrology of silicate inclusions in the Miles IIE iron. Proceedings, 9th NIPR Symposium. pp. 143–173.

Ikeda Y., Ebihara M., and Prinz M. 1997. Petrology and chemistry of the Miles IIE iron. I: Description and petrology of twenty new silicate inclusions. *Antarctic Meteorite Research* 10:355–372.

Irving A. J., Bunch T. E., Kuehner S. M., Herd C. D. K., Gellissen M., Lapen T. J., Rumble D., and Pitt D. 2011. Petrologic, elemental and isotopic characterization of shock-melted enriched ultramafic poikilitic shergottite Northwest Africa 6342 (abstract #1612). 42nd Lunar and Planetary Science Conference. 1612.

Jarosewich E., Nelen J. A., and Norberg J. A. 1980. Reference samples for electron microprobe analysis. *Geostandards Newsletter* 4:43–47.

Kamenetsky V. S., Charlier B., Zhitova L., Sharygin V., Davidson P., and Feig S. 2013. Magma chamber–scale liquid immiscibility in the Siberian Traps represented by melt pools in native iron. *Geology* 41:1091–1094.

Kleine T., Mezger K., Palme H., Scherer E., and Münker C. 2005. Early core formation in asteroids and late accretion of chondrite parent bodies: Evidence from ^{182}Hf–^{182}W in CAIs, metal-rich chondrites, and iron meteorites. *Geochimica et Cosmochimica Acta* 69:5805–5818.

Lofgren G. 1989. Dynamic crystallization of chondrule melts of porphyritic olivine composition: Textures experimental and natural. *Geochimica et Cosmochimica Acta* 53:461–470.

McCoy T. J. 1995. Silicate-bearing IIE irons: Early mixing and differentiation in a core-mantle environment and shock resetting of ages. *Meteoritics* 30:542–543.

McCoy T. J., Scott E. R. D., Jones R. H., Keil K., and Taylor G. J. 1991. Composition of chondrule silicates in LL3-5 chondrites and implications for their nebula history and parent body metamorphism. *Geochimica et Cosmochimica Acta* 55:601–619.

McKay G. A., Kridelbaugh S. J., and Weill D. F. 1973. The occurence and origin of schreibersite-kamacite intergrowths in microbreccia 66055. Proceedings, 3rd Lunar Science Conference. pp. 811–818.

Metzler K., Bischoff A., Greenwood R. C., Palme H., Gelissen M., Hopp J., Franchi I. A., and Trieloff M. 2011. The L3-6 chondritic regolith breccia Northwest Africa (NWA) 869: (I) Petrology, chemistry, oxygen isotopes and Ar-Ar age determinations. *Meteoritics & Planetary Science* 46:652–680.

Mittlefehldt D. W. and Lindstrom M. M. 2001. Petrology and geochemistry of Patuxent Range 91501, a clast-poor impact melt from the L-chondrite parent body and Lewis Cliff 88663, an L7 chondrite. *Meteoritics & Planetary Science* 36:439–457.

Mittlefehldt D. W., McCoy T. J., Goodrich C. A., and Kracher A. 1998. Non-chondritic meteorites from asteroidal bodies. In *Planetary materials*, edited by Papike J. J. Albuquerque, New Mexico: Mineralogical Society of America. pp. 4.1–4.195.

Nakamura N., Fujiwara T., and Nofda S. 1990. Young asteroid melting event indicated by Rb-Sr dating of Point of Rocks meteorite. *Nature* 345:51–53.

Niemeyer S. 1980. I-Xe and ^{40}Ar-^{39}Ar dating of silicate from Weekeroo Station and Netschaëvo IIE iron meteorites. *Geochimica et Cosmochimica Acta* 44:33–44.

Norman M. D. and Mittlefehldt D. W. 2002. Impact processing of chondritic planetesimals. Siderophile and volatile element fractionation in the Chico L chondrite. *Meteoritics & Planetary Science* 37:329–344.

Olsen E. and Jarosewich E. 1971. Chondrules: First occurrence in an iron meteorite. *Science* 174:583–585.

Olsen E., Davis A., Clarke R. S. J., Schultz L., Weber H. W., Clayton R., Mayeda T., Jarosewich E., Sylvester P., Grossman L., Wang M.-S., Lipschutz M. E., Steele I. M., and Schwade J. 1994. Watson: A new link in the IIE iron chain. *Meteoritics* 29:200–213.

Osadchii E. G., Baryshnikova G. V., and Novikov G. V. 1981. The Elga meteorite: Silicate inclusions and shock metamorphism. Proceedings, 12th Lunar and Planetary Science Conference. pp. 1049–1068.

Poldervaart A. and Hess H. H. 1951. Pyroxenes in the crystallization of basaltic magma. *The Journal of Geology* 5:472–489.

Prinz M., Nehru C. E., Delaney J. S., Harlow G. E., and Bedell R. L. 1980. Modal studies of mesosiderites and related achondrites, including the new mesosiderite ALHA 77219. Proceedings, 11th Lunar and Planetary Science Conference. pp. 1055–1071.

Prinz M., Nehru C. E., and Delaney J. S. 1982. Sombrerete: an iron with highly fractionated amphibole-bearing Na-P silicate inclusions. Proceedings, 13th Lunar and Planetary Science Conference. pp. 634–635.

Roedder E. 1978. Silicate liquid immiscibility in magmas and in the system K_2O-FeO-Al_2O_3-SiO_2: An example of serendipity. *Geochimica et Cosmochimica Acta* 42:1597–1617.

Roedder E. 1979. Silicate liquid immiscibility in magmas. In *The evolution of the igneous rocks*, edited by Yoder H. S. Princeton, New Jersey: Princeton University Press. pp. 15–57.

Rubin A. E. 1990. Kamacite and olivine in ordinary chondrites: Intergroup and intragroup relationships. *Geochimica et Cosmochimica Acta* 54:1217–1232.

Rubin A. E. 2002. Smyer H-chondrite impact-melt breccia and evidence for sulfur vaporization. *Geochimica et Cosmochimica Acta* 66:699–711.

Rubin A. E. and Jones R. H. 2003. Spade: An H chondrite impact-melt breccia that experienced post shock annealing. *Meteoritics & Planetary Science* 38:1507–1520.

Rubin A. E., Jerde E. A., Zong P., Wasson J. T., Westcott J. W., Mayeda T. K., and Clayton R. N. 1986. Properties of the Guin ungrouped iron meteorite: The origin of Guin and of group-IIE irons. *Earth and Planetary Science Letters* 76:209–226.

Russell S. S., McCoy T. J., Jarosewich E., and Ash R. D. 1998. The Burnwell, Kentucky, low iron oxide chondrite fall: Description, classification and origin. *Meteoritics & Planetary Science* 33:853–856.

Ruzicka A. M. 2014. Silicate-bearing iron meteorites and their implications for the evolution of asteroidal parent bodies. *Chemie der Erde—Geochemistry* 74:3–48.

Ruzicka A. M. and Hutson M. 2010. Comparitive petrology of silicates in the Udei Station (IAB) and Miles (IIE) iron meteorites: Implications for the origin of silicate-bearing irons. *Geochimica et Cosmochimica Acta* 74:394–433.

Ruzicka A. M., Fowler G. W., Snyder G. A., Prinz M., Papike J. J., and Taylor L. A. 1999. Petrogenesis of silicate inclusions in the Weekeroo Station IIE iron meteorite: Differentiation, remelting, and dynamic mixing. *Geochimica et Cosmochimica Acta* 63:2123–2143.

Ruzicka A. M., Killgore M., Mittlefehldt D. W., and Fries M. D. 2005. Portales Valley: Petrology of a metallic-melt meteorite breccia. *Meteoritics & Planetary Science* 40:261–295.

Ruzicka A. M., Hutson M., and Floss C. 2006. Petrology of silicate inclusions in the Sombrerete ungrouped iron meteorite: Implications for the origin of IIE-type silicate-bearing irons. *Meteoritics & Planetary Science* 41:1797–1831.

Ryerson F. J. and Hess P. C. 1978. The role of P2O5 in silicate melts. *Geochimica et Cosmochimica Acta* 44:611–624.

Scott E. R. D. 1972. Chemical fractionation in iron meteorites and its interpretation. *Geochimica et Cosmochimica Acta* 36:1205–1236.

Scott E. R. D. 1982. Origin of rapidly solidified metal-troilite grains in chondrites and iron meteorites. *Geochimica et Cosmochimica Acta* 46:813–823.

Scott E. R. D. and Wasson J. T. 1976. Chemical classification of iron meteorites—VIII. Groups IC. IIE. IIIF and 97 other irons. *Geochimica et Cosmochimica Acta* 40:103–115.

Scott E. R. D., Clayton R. N., and Mayeda T. K. 1985. Properties and genesis of two anomalous type 3 chondrites, Suwahib (buwah) and Willaroy (abstract). 16th Lunar and Planetary Science Conference. pp. 749–750.

Scott E. R. D., Krot T. V., Goldstein J. I., and Wakita S. 2014. Thermal and impact history of the H chondrite parent asteroid during metamorphism: Constraints from metallic Fe-Ni. *Geochimica et Cosmochimica Acta* 136:13–37.

Sharp T. G. and DeCarli P. S. 2006. Shock effects in meteorites. In *Meteorites and the early solar system II*, edited by Lauretta D. and McSween H. Y. Jr. Tucson, Arizona: The University of Arizona Press. pp. 653–677.

Shaw C. S. J. and Walton E. 2013. Thermal modeling of shock melts in Martian meteorites: Implications for preserving Martian atmospheric signatures and crystallization of high-pressure minerals from shock melts. *Meteoritics & Planetary Science* 48:758–770.

Smith B. A. and Goldstein J. I. 1977. The metallic microstructures and thermal histories of severely reheated chondrites. *Geochimica et Cosmochimica Acta* 41:1061–1072.

Stöffler D. and Grieve R. A. F. 2007. Impactites. In *Metamorphic rocks: A classification and glossary of terms*, edited by Fettes D. and Desmons J. Cambridge, UK: Cambridge University Press. pp. 82–242.

Stöffler D., Keil K., and Scott E. R. D. 1991. Shock metamorphism of ordinary chondrites. *Geochimica et Cosmochimica Acta* 55:3845–3867.

Takeda H., Bogard D. D., Otsuki M., and Ishii T. 2003a. Mineralogy and Ar–Ar age of the Tarahumara IIE iron, with reference to the origin of alkali-rich materials. NIPR Annual Meeting, Tokyo, September 2003.

Takeda H., Hsu W., and Huss G. R. 2003b. Mineralogy of silicate inclusions of the Colomera IIE iron and crystallization of Cr-diopside and alkali feldspar from a partial melt. *Geochimica et Cosmochimica Acta* 67:2269–2288.

Taylor G. J. and Heymann D. 1971. Postshock thermal histories of reheated chondrites. *Journal of Geophysical Research* 76:1879–1893.

Taylor G. J., Keil K., Berkley J. L., Lange D. E., Fodor R. V., and Fruland R. M. 1979. The Shaw meteorite: History of a chondrite consisting of impact-melted and metamorphic lithologies. *Geochimica et Cosmochimica Acta* 43:323–337.

Tomkins A. G., Weinberg R. F., Schaefer B. F., and Langendam A. 2013. Disequilibrium melting and melt migration driven by impacts: Implications for rapid planetesimal core formation. *Geochimica et Cosmochimica Acta* 100:41–59.

Underwood E. E. 1970. *Quantitative stereology*. Reading, Massachusetts: Addison-Wesley Publishing Company. 274 p.

Van Roosbroek N., Debaille V., Pittarello L., Goderis S., Humayun M., Hecht L., Jourdan F., Spicuzza M., Vanhaecke F., and Claeys P. 2015. The formation of IIE iron meteorites investigated by the chondrule-bearing Mont Dieu meteorite. *Meteoritics & Planetary Science* 50:1173–1196.

Visser W. and Koster van Groose A. F. 1979. Effects of P_2O_5 and TiO_2 on liquid-liquid equilibria in the system K_2O-FeO-Al_2O_3-SiO_2. *American Journal of Science* 279:970–988.

Walton E. L. and Herd C. D. K. 2007. Dynamic crystallization of shock melts in Allan Hills 77005: Implications for melt pocket formation in Martian meteorites. *Geochimica et Cosmochimica Acta* 71:5267–5285.

Wasserburg G. J., Sanz G. J., and Bence A. E. 1968. Potassium-feldspar phenocrysts in the surface of Colomera, an iron meteorite. *Science* 161:684–687.

Wasson J. T. and Wang J. 1986. A nonmagmatic origin of group-IIE iron meteorites. *Geochimica et Cosmochimica Acta* 50:725–732.

Watson E. B. 1976. Two-liquid partition coefficients: Experimental data and geochemical implications. *Contributions to Mineralogy and Petrology* 56:119–134.

Whitlock R., Lewis C. F., Clark J. C., and Moore C. B. 1991. The Cerro Los Calvos and La Banderia chondrites. *Meteoritics* 26:169–170.

Yamaguchi A., Scott E. R. D., and Keil K. 1999. Origin of a unique impact-melt rock—The L-chondrite Ramsdorf. *Meteoritics & Planetary Science* 34:49–59.